New Journal of Physics
The open access journal at the forefront of physics
Deutsche Physikalische Gesellschaft DPG | IOP Institute of Physics

Hydration layers trapped between graphene and a hydrophilic substrate

M Temmen[1], O Ochedowski[2], M Schleberger[2], M Reichling[1] and T R J Bollmann[1,3]

[1] Fachbereich Physik, Universität Osnabrück, Barbarastraße 7, 49076 Osnabrück, Germany
[2] Fakultät für Physik and CeNIDE, Universität Duisburg-Essen, 47048 Duisburg, Germany
E-mail: tbollman@uos.de

Received 14 January 2014, revised 12 March 2014
Accepted for publication 3 April 2014
Published 21 May 2014

New Journal of Physics **16** (2014) 053039

doi:10.1088/1367-2630/16/5/053039

Abstract

Graphene is mechanically exfoliated on $CaF_2(111)$ under ambient conditions. We demonstrate the formation of a several monolayer thick hydration layer on the hydrophilic substrate and its response to annealing at temperatures up to 750 K in an ultra-high vacuum environment. Upon heating, water is released, however, it is impossible to remove the first layer. The initially homogeneous film separates into water-containing and water-free domains by two-dimensional Ostwald ripening. Upon severe heating, thick graphene multilayers undergo rupture, while nanoblisters confining sealed water appear on thinner sheets, capable of the storage and release of material. From modeling the dimensions of the nanoblisters, we estimate the graphene/$CaF_2(111)$ interfacial adhesion energy to be 0.33 ± 0.13 J m^{-2}, thereby viable for polymer-assisted transfer printing.

Keywords: graphene, diffusion of adsorbates, kinetics of coarsening and aggregation, liquid–solid interface structure, atomic force microscopy, Kelvin probe force microscopy

[3] Current address: Inorganic Materials Science, MESA$^+$ Institute for Nanotechnology, Physics of Interfaces and Nanomaterials, P.O. Box 217, NL-7500AE Enschede, The Netherlands.

1. Introduction

Since the demonstration of isolated graphene sheets exfoliated from graphite in 2004 [1], graphene has attracted enormous interest due to its unique properties of very high electrical and thermal conductivity, mechanical strength, chemical inertness, particle impermeability and its enormous elasticity allowing it to stretch by 20% [2, 3]. The preparation by mechanical exfoliation [1] results in large graphene flakes of high quality, however, the ambient conditions during preparation are of great influence on the properties of graphene [4]. Exfoliation under ambient conditions generally results in uncontrolled electronic properties, however, it might also be beneficial for specific applications [5]. It is commonly assumed that a thin water layer is formed when exposing hydrophilic surfaces to the ambient atmosphere, which can be captured under the impermeable graphene layer [6–13]. Such confined interfacial layers have been suggested to be used for the storage of material in (nano)bubbles [14] of which the curvature can be controlled [5].

Here, we identify and qualitatively describe the hydration layer confined between mechanically exfoliated graphene and a well characterized insulating hydrophilic substrate, namely CaF_2(111). Using non-contact atomic force microscopy (NC-AFM) and Kelvin probe force microscopy (KPFM), we determine the graphene sheet thicknesses and the thickness of the intercalated water film. By heating the system, we demonstrate the decay of the hydration layer by the release of water and Ostwald ripening, concentrating water in direct contact to the substrate. Upon further heating in an attempt to remove the first hydration layer, we discover that it is virtually impossible to completely release the heavily trapped water. Instead, we create nanoblisters filled with water molecules for thinner graphene sheet thicknesses, while thicker graphene sheets are ruptured to release the pressure built up in the blister by evaporation of trapped water. This points to a fundamental impossibility to drive the first hydration layer on a hydrophilic substrate out of the confined space without destruction of the graphene sheet.

The investigation starts with the inspection of the as-prepared graphene flake shown in figure 1. We then attempt to remove the confined water by annealing to 400 K and 600 K as shown in figures 3 and 4. Annealing up to 600 K reveals the decay of hydration layers as well as the rearrangement of the first hydration layer. In a final attempt to remove the remaining water in the first hydration layer by annealing at 750 K, the water is rather driven into nanoblisters as seen in figure 5.

2. Methods

Graphene is exfoliated from a highly oriented pyrolytic graphite crystal (Momentive Performance Materials, Columbus, OH, USA) under ambient conditions applying a standard recipe [1] on a CaF_2(111) crystal likewise cleaved under ambient conditions. After exfoliation, the flakes are initially inspected by an optical microscope, where they appear with reasonable contrast [15], and are then characterized by Raman microscopy to confirm their identity as single layer graphene (SLG), bilayer graphene (BLG) or few layer graphene (FLG) using the G and 2D bands [16–18]. NC-AFM measurements are performed with a well characterized [19–21] UHV 750 NC-AFM system (RHK Technology, Troy, MI, USA) in an ultra-high vacuum (UHV) chamber with a base pressure below 1×10^{-10} mbar. Force sensors used are commercial type NCH Si cantilevers (Nanosensors, Neuchatel, Switzerland) with an

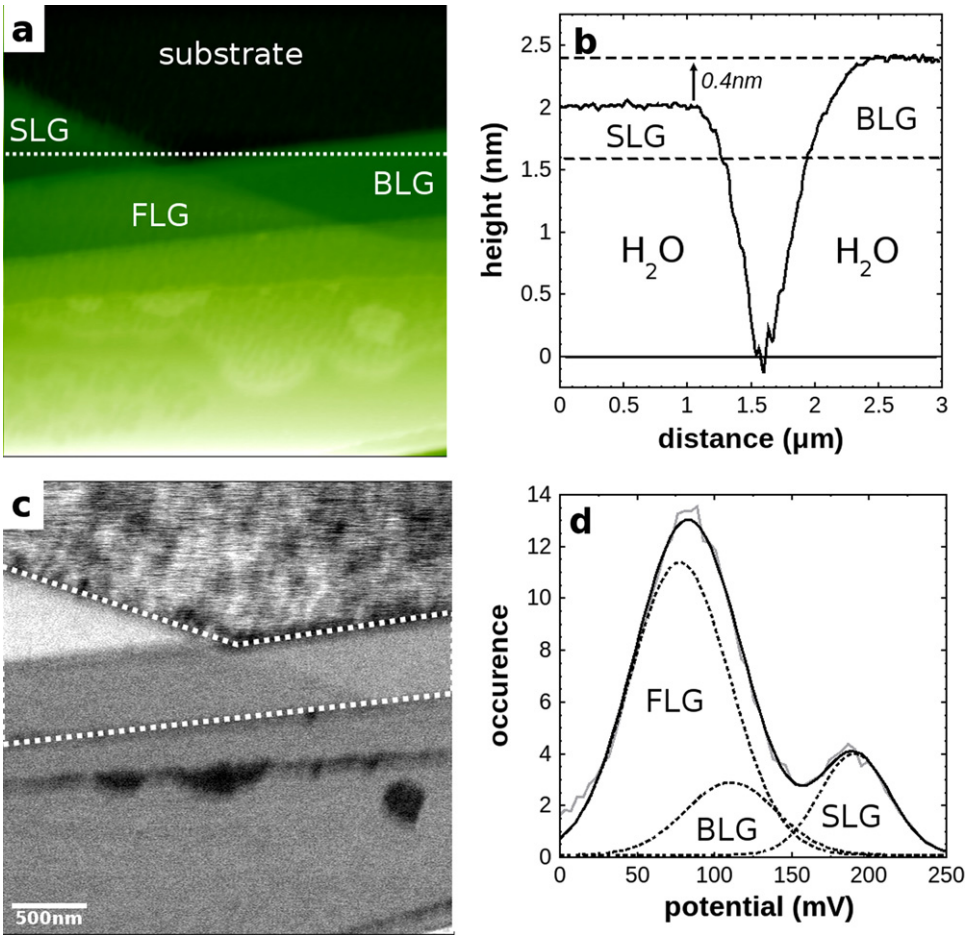

Figure 1. (a) NC-AFM image of a graphene flake containing SLG, BLG and FLG sheets. (b) The line-profile taken along the dotted line in figure 1(a) reveals the interlayer distance for graphene sheets as well as the thickness of the confined water film. (c) The SLG, BLG and FLG sheets can be identified from their unique contrast in the corresponding KPFM image taken simultaneously to the topographic image. (d) From a statistical analysis of the potential, found in the area enclosed by the dotted line in (c), the potential for FLG (77 ± 30 mV), BLG (110 ± 30 mV) and SLG (190 ± 20 mV) can be extracted from a fit of normal distributions to the observed occurence.

eigenfrequency of $f_0 \simeq 300$ kHz. KPFM imaging [22–24] is performed simultaneously by applying an AC voltage of 1 V_{pp} amplitude at a frequency of 1.2 kHz added to the DC bias regulated to minimize electrostatic forces. By the simultaneous use of NC-AFM and KPFM, we are able to yield correct height information and to identify the different graphene sheet thicknesses as well as the thickness of the confined water film. Images are compensated for piezo creep and drift as well as for scanner bow by applying common plane subtraction and (facet) leveling algorithms implemented in the Gwyddion software package [25] to topographic data. The sample temperature is measured by a thermocouple clamped by a washer onto the edge of the substrate surface, therefore, the surface temperature might be slightly underestimated.

3. Results and discussion

Figures 1(a) and (c) show a typical example of the topography and local potential at the periphery of a graphene flake. Line-profiles (see figure 1(b)) reveal the interlayer distance of graphene sheets, here 0.4 ± 0.1 nm between SLG and BLG, in agreement with the interlayer distance found for graphite stacking [26–28]. The line-profile also demonstrates the exceptional height for SLG with respect to the underlying substrate. A typical height for SLG above the substrate is 2.0 ± 0.2 nm due to the interfacial layer. Determined in several experiments, the confined water film is found to have a height of typically 1.5 nm, where figure 1(a) is a representative example. The contrast in KPFM, shown in figure 1(c), is used to distinguish the thinnest sheet thicknesses from each other and from FLG by methods well established in the literature [29, 30] and in agreement with our characterization by Raman microscopy. Figure 1(d) shows a histogram of the surface potential values taken from the area enclosed by the dotted line in figure 1(c). We find that the areas containing SLG, BLG and FLG are in proportions of 1:1:3. We take these area ratios into account when fitting three normal distributions to the data to identify the respective potential values. The potential for FLG sheets is the same as that for a graphite stack of ∼50 layers found on the sample. For BLG we find a potential increase of 30 mV with respect to thicker graphene sheets, and SLG increases the potential by another 80 mV.

To understand the exceptional height for SLG, we analyse the role of ambient conditions during the preparation of the $CaF_2(111)$ substrate and the subsequent graphene exfoliation. The cleavage of $CaF_2(111)$ in ambient is known to result in atomic scale roughness due to the reaction of the surface with constituents of the surrounding air [31]. Upon stronger water exposure, NC-AFM imaging further reveals the formation of thin water films on the hydrophilic $CaF_2(111)$ surface [32] similar to observations for $BaF_2(111)$ [32, 33]. Although $BaF_2(111)$ and $CaF_2(111)$ are similar in crystal structure and binding energies for adsorbed water molecules, ice Ih water adlayers are not observed on the latter, due to the lattice mismatch with the basal plane of ice Ih water adlayers and the weak interaction of graphene with the water molecules [13]. Respective experimental observations have been confirmed by atomistic simulations [34] and electronic structure calculations [35–38] yielding an energetic preference for associative water adsorption on $CaF_2(111)$. The partial dissociation (O+OH) of water on the ideal $CaF_2(111)$ surface costs over 3 eV more than molecular adsorbed water, and in the presence of a significant amount of neutral vacancies the additional cost is only 0.16 eV [37]. The thermal treatment described further on should easily exceed the latter barrier in the case of an unanticipated significant amount of neutral vacancies, resulting in molecular adsorbed water. Not surprisingly, the relative humidity (RH) of the surrounding air plays an important role for the water coverage and the degree of surface degradation [6, 10, 13, 33]. The formation of a thin water film, its confinement by mechanical exfoliation of graphene [6, 10, 12, 13], and its growth, is depicted in the cartoon of figure 2. Once formed, a confined water film is stabilized by the strong van der Waals forces acting between water, the graphene sheet and the underlying substrate. The underlying mechanisms are Langmuir adsorption followed by capillary forces driving water underneath the graphene sheet that can be assumed to be hydrophilic under the given conditions [39]. For an estimate of the areal coverage of the water film on $CaF_2(111)$ before graphene exfoliation, we determine the RH in our laboratory to be 30 ± 5%, similar to conditions reported in [32] and note that several minutes pass between cleavage and exfoliation,

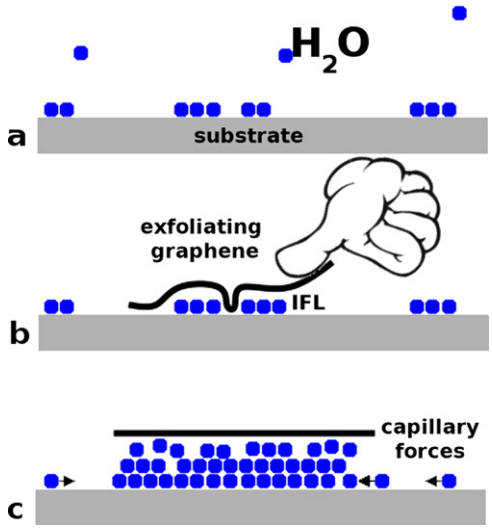

Figure 2. Illustration of processes occuring during exfoliation of graphene under ambient conditions. (a) Adsorption of water from the air onto a freshly cleaved $CaF_2(111)$ substrate. (b) Mechanical exfoliation results in the confinement of a water film between the substrate surface and the graphene film. (c) Due to capillary forces, the water film confined between the graphene and substrate grows in areal coverage and thickness by the uptake of water from surface regions adjacent to the graphene flake.

similar to the exposure of 'a few minutes' described in [32]. From the images shown in [32], where the sample has been cleaved in ambient and exposed to air for a few minutes, we derive an estimate of the hydration layer areal coverage of about 10%. Modeling the coverage as a function of time assuming Langmuir adsorption [40], we find that three hours of exposure to the ambient air are needed to develop a water film covering 80% of the surface. Water adsorption on the $CaF_2(111)$ surface followed by graphene exfoliation within minutes after cleavage is, therefore, described by the initial linear regime of the Langmuir adsorption isotherm and will confine a water film of several (tens of) percent of areal coverage.

The submonolayer coverage yielded during the exfoliation process can thus by far not explain the exceptional height measured for the water film underneath SLG. To explain this observation, we recall that after exfoliation, the sample is kept in ambient for approximately 36 h. We suggest the transport of adsorbed water by diffusion on the $CaF_2(111)$ surface towards the graphene flake during this time in ambient after exfoliation. Once a film is formed, water from the surface is driven underneath the graphene due to capillary forces as illustrated in figure 2(c). From figure 1(a), it is clear that graphene sheets are not floating on a water film extending beyond the area of the graphene flake, what we would expect for hydrophobic graphene. The water film being confined underneath the graphene flake is rather indicative of the hydrophilic nature of the graphene sheet in our case, which is a plausible assumption according to recent findings in the literature [39].

In an attempt to remove the interfacial layer, we anneal the sample at elevated temperatures. Figure 3(a) shows two FLG sheets of similar height after annealing to 400 K. Annealing results in the decay of the confined thick water film, leaving a thin hydration layer with different height levels. Figure 3(a) exhibits all relevant height levels forming different contrast patterns on the two adjacent FLG sheets, of which the FLG flake in the top right region

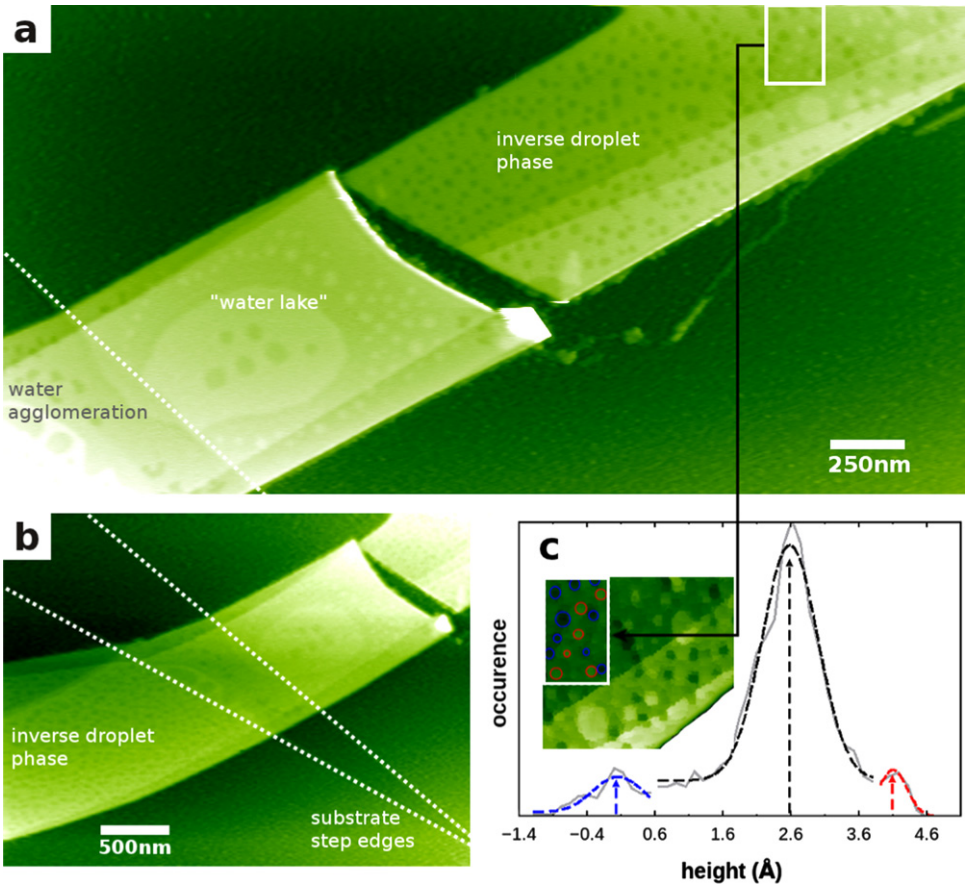

Figure 3. (a) NC-AFM image of an FLG flake heated to 400 K. The annealing results in the decay of the interfacial layer. The inverse droplet phase contains domains of graphene in contact with the substrate and domains with a thin hydration layer in between graphene and the substrate. The agglomeration of water found for the flake at the bottom left results from the nearby substrate step edge also seen in the larger scale image (b) where steps are marked by dotted lines. (c) From the height histogram of the area marked by the box in (a), the fit of three normal distributions reveals the two height levels of the first two hydration layers at 2.6 ± 0.4 Å and 1.5 ± 0.2 Å, marked by corresponding blue and red circles in the inset. A Kuwahara filter is applied to this area for image analysis to suppress noise on the terrace and to sharpen steps, thereby improving the contrast between height levels [41].

shows the thinnest hydration layers that are rearranged due to the decay of water. To understand the two different contrast patterns present in the rectangle of figure 3(a), we determine the height distribution shown in figure 3(c). The resulting histogram shows three distinct peaks, each representing a normal distribution. The lowest peak corresponds to water-free domains encircled in blue in the inset of figure 3(c). They are surrounded by water from the first hydration layer raising the graphene sheet 2.6 ± 0.4 Å higher, which is represented by the black dashed line in figure 3(c). The height of the first hydration layer is in agreement with atomistic molecular dynamics calculations [37, 38], predicting an ordered water layer on $CaF_2(111)$ with molecules situated 2.6 Å above the surface calcium ions [38]. The small circular depressions found in the area marked in figure 3(a) are, therefore, identified as patches free of intercalated

water where the graphene film is in direct contact with the $CaF_2(111)$ substrate. These patches, free of intercalated water, are denoted further-on as water-free domains and the hydration layer containing such domains as an inverse droplet phase in figure 3(a).

Besides this inverse droplet phase, another layer on top of the first hydration layer can be discerned as illustrated in the inset of figure 3(c) by red circles corresponding to the highest peak in the histogram of figure 3(c). This second water layer is situated 1.5 ± 0.2 Å above the first water layer, in agreement with atomistic molecular dynamics calculations predicting a second ordered water layer where the oxygen atoms of the water molecules are situated above surface fluorine ions [38]. This calculation also predicts that the lateral order of the third layer (and higher layers) is quite low. Mild annealing is, therefore, believed to result in the decay of weakly bound water layers being separated more than 1 nm from the surface [38], in accordance with observations made in figure 3(a) where the second layer has almost vanished for the flake in the top right region.

The flake at the bottom left shows a different behavior. Apart from one large 'water lake' in the center (mainly), small circular mounds can be observed. A detailed analysis reveals the small pits at the flakes edges to be about 1.5 Å in depth, in agreement with a second hydration layer, while the mounds are interpreted as agglomerations of water in the third layer, 1.9 Å above the water layer below in accordance with the prediction of water layers attaining a more bulk-like behavior for increased distance to the substrate surface [38]. The triple layer (F^-–Ca^{2+}–F^-) substrate step at the bottom left marked by the dotted line apparently influences the diffusion of water. Intralayer diffusion, which is anticipated to be slower than the diffusion across the terrace, combined with pinning at surface defects might be the cause of the 'water lake' pinned at the substrate step. This is confirmed by a zoom-out image of this area, shown in figure 3(b), where the same and another substrate step are marked by dotted lines. At the bottom left region of figure 3(b), the inverse droplet phase is found as well, while large agglomerates dominate the lower terrace between the two substrate steps.

The first hydration layer is persistent to heating and hardly shows any reduction in its areal coverage. However, it is rearranged by two-dimensional Ostwald ripening of the water-free domains when raising the annealing temperature as illustrated in figure 4. Annealing at 600 K results in patches corresponding to the first hydration layer, while water from all other layers has been driven out. Imaging several different graphene flakes annealed to 600 K shows the trend that the average size of water-free domains increases, while the number of domains decreases as a function of temperature. Notably, the areal coverage of the first water layer turns out to be rather persistent to heating, being 80 ± 2% at 400 K and 78 ± 2% at 600 K. The conservation of mass together with the increase of the water-free mean domain area and the decrease of the number of domains implies a rearrangement of the first hydration layer. Typical examples of the topography at 400 K and 600 K showing this phenomenon are shown as insets in figure 4.

To determine the kinetics involved in the rearrangement, we measure the number and average size of water-free domains for three images at two temperatures, namely 400 K and 600 K. The mean area of water-free domain areas and the mean number of water-free domains per unit area are plotted in figure 4. The domain mean area measured is described by a single-exponential (Arrhenius-like) behavior, where the domain area is set to vanish at 0 K in figure 4. This describes a process where the water-free domains compete with the first hydration layer. In our kinetic model, initial vacancy creation in the first hydration layer is followed by two-

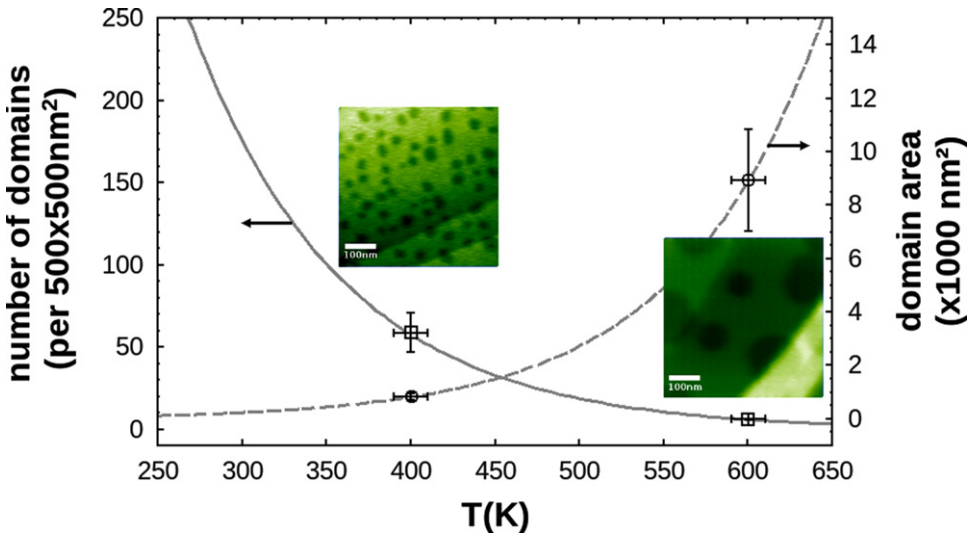

Figure 4. The mean area of water-free domains and the average number of domains in images (500×500 nm^2 in size) exemplifying the effect of the ripening process at temperatures of 400 K and 600 K. Images are analyzed by adaptive thresholding [42] to correct for gradients across the images, and by applying Otsu's method [43] separating the pixels into two classes (water-free domains and first hydration layer) separated by a threshold intensity. This process is followed by applying common erosion and dilation filters [41]. The solid and dashed lines are a fit of an Arrhenius curve to the data points.

dimensional Ostwald ripening, yielding a strong phase separation. The Ostwald ripening of water-free domains is driven by the minimization of the phase-boundary area as it is observed in a variety of similar systems [44]. For increasing temperature, the diffusion of water molecules results in the growth of larger water-free domains at the expense of smaller ones. The strain, resulting from elastic deformations at the border between the substrate and the confined first hydration layer, changes the elastic energy being minimized as the net contact boundary is decreasing and is thereby driving the ripening process [45]. The growth of the water-free domains is controlled by the diffusion barrier of the vacancies in the first hydration layer, resulting in an Arrhenius-like temperature dependence of the domain size as found in figure 4. The NC-AFM images represent, therefore, snapshots of intermediate stages of Ostwald ripening, for a system that is not yet in thermodynamic equilibrium.

In an attempt to further increase the area of the water-free domains, we anneal the sample at a temperature of 750 K, where a typical resulting topography is shown in figure 5(a). Image and line-profile analysis reveals small protrusions on the thinner graphene sheets in the center of the image, ranging in size from 0.3 to 1.6 nm in height and from 80 to 180 nm in diameter; see figure 5(b). The protrusions exhibit an areal coverage of ≈8% on the thinner graphene sheets. We interpret these findings in the following way. Due to the Ostwald ripening in the first hydration layer, larger water-free domains are formed at higher temperatures. The boundaries of these water-free domains eventually meet and join, a process greatly reducing the total strain energy in the system. Due to the increased temperature, the water molecules contained in the first hydration layer patches evaporate and pressure is released by the creation of nanoblisters. Upon cooling, the water vapor condenses into liquid-filled nanoblisters having a much smaller volume (height) than the vapor-filled nanoblisters. For one example, we plot in figure 5(c) a line-profile of the spherical cap measured at RT together with the modeled spherical cap at

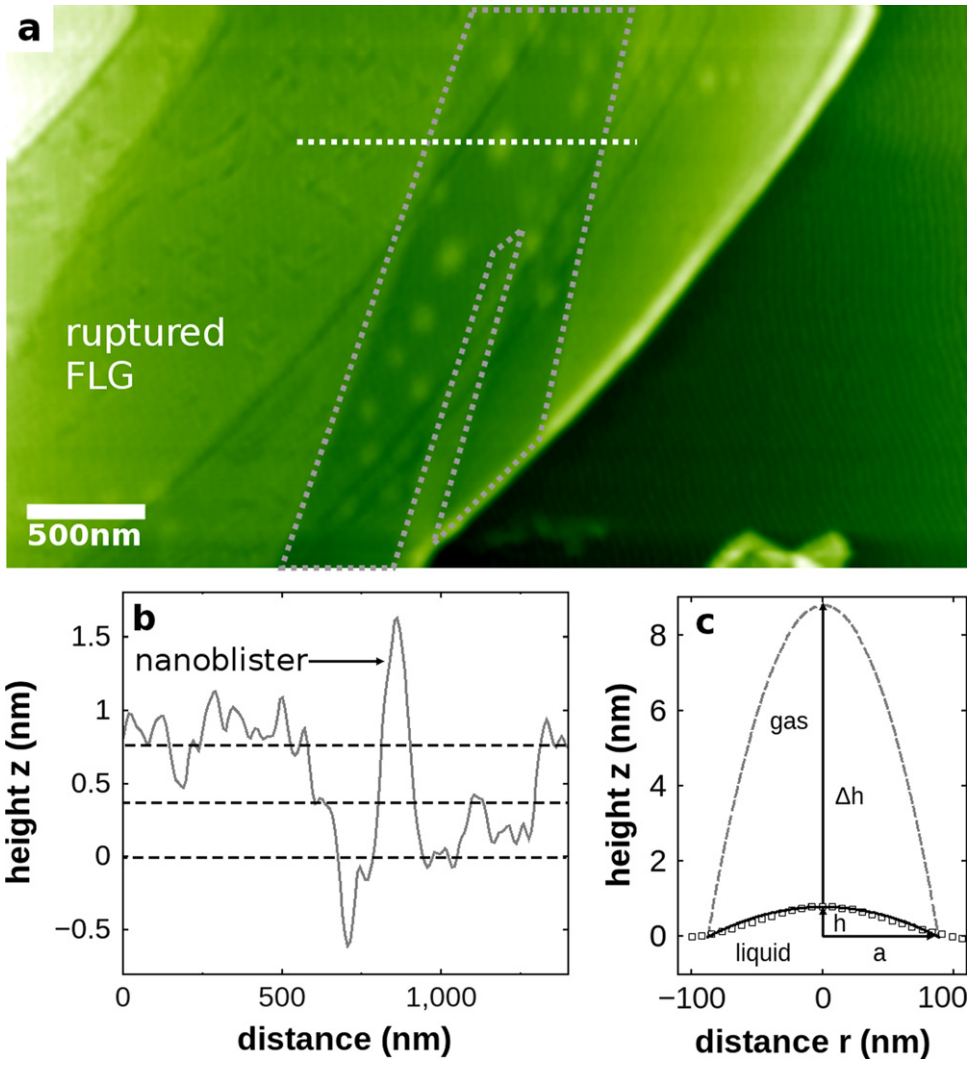

Figure 5. (a) NC-AFM image of an FLG flake heated to 750 K. The annealing results in the creation of nanoblisters for thinner graphene sheets, whereas thicker graphene sheets show rupture in the form of troughs of several nm depth. The line-profile (b) corresponding to the dotted line in (a) reveals the nanoblister found on the thinner graphene sheet in the middle of the image. The interlayer distance between subsequent graphene sheets of 0.4 nm is marked by dashed lines. (c) The central deflection h and radius a of the nanoblisters are deduced from a fit of a spherical cap to the height profile. This yields the volume of the liquid water in the blister at RT. The nanoblisters central deflection $(h + \Delta h)$ for a nanoblister containing evaporated water is calculated assuming that no delamination occurs during the phase transition [46].

750 K, discussed below. While thin graphene sheets show nanoblisters, thicker graphene sheets show rupture along the edges of water-free domains as seen in the left part of figure 5(a). The nanoblisters rupture in this case as the thicker graphene sheets have a reduced hardness [47–49] and are not able to accommodate the pressure built up during water evaporation.

For a quantitative analysis of the nanoblisters, we model them as spherical caps, and calculate the sum over the volumes ($\Sigma_n V_n^{RT}$) of the n protrusions seen in figure 5(a) at RT. For

the volume of an individual blister we assume

$$V_n^{RT} = \frac{\pi h_n}{6}\left(3a_n^2 + h_n^2\right), \tag{1}$$

where h_n is the central deflection and a_n is the radius of the spherical cap. Figure 5(c) shows that the spherical cap is a decent approximation that can, however, not accurately describe the blister at its edge with its zero-slope boundary. We find $\Sigma_n V_n^{RT}$ to correspond to a 63–71% areal coverage of a single hydration layer underneath the thinner graphene sheet marked by the (grey) dashed line in figure 5(a).

Measuring the dimensions of the nanoblisters taking the elastic properties of graphene into account, we can estimate the adhesion energy γ for graphene on $CaF_2(111)$. Analytical methods such as a membrane analysis [50] are used to determine the number of gas molecules inside the blister and its internal pressure. From this we derive the adhesion energy between graphene and the substrate assuming the ideal gas law. Figure 5(c) shows the spherical cap with a central deflection h and radius a, containing the liquid water measured at RT. To estimate an upper limit for the adhesion energy, we assume the nanoblister to grow in height rather than increasing its lateral extension by delamination, as graphene is in contact with the substrate beyond the circumference of the blister and known to have a very high elasticity, easily enabling strong deformation upon pressure increase before delamination sets in [46]. We approximate the nanoblister as a spherical cap filled with gas at a temperature of 750 K and describe the deflection profile upon evaporation by [50]

$$z(r) = (h + \Delta h)\left(1 - \frac{r^2}{a^2}\right), \tag{2}$$

with $(h + \Delta h)$ being the increased central deflection, see figure 5(c). The volume of the nanoblister at elevated temperature is then described as

$$V_n^{750K} = \frac{\pi\left(h_n + \Delta h_n\right)}{6}\left(3a_n^2 + \left(h_n + \Delta h_n\right)^2\right). \tag{3}$$

By conservation of the number of molecules N in the nanoblister, calculated from the volume of the blister containing liquid at RT (V_n^{RT}), the central deflection $(h + \Delta h)$ at a given temperature T is determined as

$$(h + \Delta h) = \sqrt[4]{\frac{2Nk_BT\phi a^2}{\pi E_{2D}}}, \tag{4}$$

where T = 750 K and E_{2D} = 353 N m^{-1} [47] is the 2D Young's modulus of (monolayer) graphene. Note that the Young's modulus E_{2D} has been found to be similar for SLG, BLG and trilayer graphene, and equal to the Young's modulus for bulk graphite [48]. Knowing the Poisson ratio for graphene $\nu = 0.16$ [50], we can calculate $\phi(\nu) = \frac{72\left(1-\nu^2\right)}{8\left(23+18\nu-3\nu^2\right)}$ as described elsewhere [50][4].

[4] Note that herein the UHV background pressure p_0 outside the nanoblister is many orders of magnitude smaller than the pressure inside. Therefore, the contribution of the term $p_0 a^2 h$ in [50] can be neglected.

The adhesion energy γ for the graphene/substrate interface can be determined as

$$\gamma = \frac{5E_{2D}\left(h + \Delta h\right)^4}{8\phi a^4}, \tag{5}$$

as described in [50]. The calculated adhesion energies determined for all 16 nanoblisters shown in figure 5(a), yield a normal distribution with a mean of 0.33 J m^{-2} and a standard deviation of 0.13 J m^{-2}. The adhesion energy between graphene and various substrates is found to range over three orders of magnitude [51], from 0.007 J m^{-2} for graphene on PDMS [52] to 0.72 J m^{-2} for graphene on copper [53]. Hence, the value found for graphene/CaF_2(111) is on the high side and it should be easy to, for instance, transfer graphene from a PDMS stamp to a CaF_2(111) substrate [54–56].

Note that the estimated adhesion energy is an upper limit and might be overestimated, due to the assumption that the radius a will stay constant upon growth and no delamination will occur. Small errors in the radius a might, however, lead to substantial deviations in the adhesion energy γ as can be seen from analyzing the error propagation in equation (5). However, the strain in the graphene sheet (∼2%), calculated by the relative increase in the spherical cap area when growing the nanoblister by Δh, can be considered rather small to its elasticity, allowing it to stretch by 20% [2, 3]. An analysis of the internal pressure required for delamination, taking the determined graphene/CaF_2(111) adhesion energy into account [46], reveals a critical interal pressure for outward delamination of ≈43 MPa, which is an order of magnitude beyond the internal pressure present in our model [50].

Next to the region of nanoblisters, the thicker graphene sheets on the left in figure 5(a) show a rupture of graphene, appearing in the form of deep trough-like structures with a depth that is hard to be determined due to the small width (∼50 nm) of the troughs. The depth is, however, clearly more than 2 nm, corresponding to more than five graphene layers. We anticipate these structures to result from pressure bursts due to boiling in the confined layer, causing rupture at the edge between the water-free domains and the adjacent confined first hydration layer. As the hardness/strength decreases for increasing graphene sheet thickness [47–49], the thicker graphene sheets are ruptured, while the thinner ones can accommodate the pressure in the nanoblisters. Having nanoblisters next to the rupture of graphene sheets two layers thicker will occur only in a narrow temperature range where the temperature is such that for the thinner sheet, the pressure inside the nanoblister can be accommodated, while the thicker sheet is unable to withstand the pressure.

4. Conclusion

In conclusion, we find that the ambient conditions during mechanical exfoliation of graphene on a hydrophilic substrate are of paramount importance for the understanding of the graphene/substrate system, as an interfacial hydration layer of considerable thickness is formed. The obtained results demonstrate both the role of the preparation conditions on graphene, and the importance of control over the behavior of confined material. One can reduce the interfacial thickness by thermal treatment, however, this introduces a phase separation between layers of different thickness and it is practically impossible to completely drive the first hydration layer out of the confined space. The residual first hydration layer will, therefore, always influence the

graphene's properties. We demonstrate the possibility to condense water into nanoblisters by accelerating Ostwald ripening, yielding a separation of void and liquid-filled phases. Such nanoblisters are found to be very stable and are, in fact, suitable candidates for the storage of molecular material. For instance, by thermal treatment one could rupture the blister and release the stored material. This provides the conceptual basis for a graphene-based nanosystem capable of both the storage and the release of chemicals in an aqueous environment. From the dimensions of the nanoblisters we can, furthermore, determine the adhesion energy between graphene and the $CaF_2(111)$ surface, which is important to know for an evaluation of the feasibility of transferring graphene to dielectric surfaces for future applications.

Acknowledgments

This work was supported by the SPP 1459 of the Deutsche Forschungsgemeinschaft. MT gratefully appreciates support from the Hans-Mühlenhoff-Stiftung. We thank Pavel B Sorokin and Liubov Antipina for useful discussions. TRJB thanks Adam S Foster for stimulating discussions.

References

[1] Novoselov K S, Geim A K, Morozov S V, Jiang D, Zhang Y, Dubonos S V, Grigorieva I V and Firsov A A 2004 Electric field effect in atomically thin carbon films *Science* **306** 666–9

[2] Soldano C, Mahmood A and Dujardin E 2010 Production, properties and potential of graphene *Carbon* **48** 2127–50

[3] Singh V, Joung D, Zhai L, Das S, Khondaker S I and Seal S 2011 Graphene based materials: past, present and future *Prog. Mater. Sci.* **56** 1178–271

[4] Song J-E, Ko T-Y and Ryu S-M 2010 Raman spectroscopy study of annealing-induced effects on graphene prepared by micromechanical exfoliation *Bull. Korean Chem. Soc.* **31** 2679–82

[5] Georgiou T, Britnell L, Blake P, Gorbachev R V, Gholinia A, Geim A K, Casiraghi C and Novoselov K S 2011 Graphene bubbles with controllable curvature *Appl. Phys. Lett.* **99** 093103

[6] Xu K, Cao P and Heath J R 2010 Graphene visualizes the first water adlayers on mica at ambient conditions *Science* **329** 1188–91

[7] Cao P, Xu K, Varghese J O and Heath J R 2011 The microscopic structure of adsorbed water on hydrophobic surfaces under ambient conditions *Nano Lett.* **11** 5581–6

[8] He K T, Wood J D, Doidge G P, Pop E and Lyding J W 2012 Scanning tunneling microscopy study and nanomanipulation of graphene-coated water on mica *Nano Lett.* **12** 2665–72

[9] Komurasaki H, Tsukamoto T, Yamazaki K and Ogino T 2012 Layered structures of interfacial water and their effects on Raman spectra in graphene-on-sapphire systems *J. Phys. Chem.* C **116** 10084–9

[10] Lee M, Choi J, Kim J-S, Byun I-S, Lee D, Ryu S, Lee C and Park B 2012 Characteristics and effects of diffused water between graphene and a SiO_2 substrate *Nano Res.* **5** 710–7

[11] Severin N, Lange P, Sokolov I M and Rabe J P 2012 Reversible dewetting of a molecularly thin fluid water film in a soft graphene/mica slit pore *Nano Lett.* **12** 774–9

[12] Shim J, Lui C H, Ko T Y, Yu Y-J, Kim P, Heinz T F and Ryu S 2012 Water-gated charge doping of graphene induced by mica substrates *Nano Lett.* **12** 648–54

[13] Verdaguer A, Segura J J, Lopez-Mir L, Sauthier G and Fraxedas J 2013 Communication: growing room temperature ice with graphene *J. Phys. Chem.* **138** 121101

[14] Stolyarova E *et al* 2009 Observation of graphene bubbles and effective mass transport under graphene films *Nano Lett.* **9** 332–7
[15] Akcöltekin S, Kharrazi M E, Köhler B, Lorke A and Schleberger M 2009 Graphene on insulating crystalline substrates *Nanotechnology* **20** 155601
[16] Malard L M, Pimenta M A, Dresselhaus G and Dresselhaus M S 2009 Raman spectroscopy in graphene *Phys. Rep.* **473** 51–87
[17] Bukowska H, Meinerzhagen F, Akcöltekin S, Ochedowski O, Neubert M, Buck V and Schleberger M 2011 Raman spectra of graphene exfoliated on insulating crystalline substrates *New J. Phys.* **13** 063018
[18] Ferrari A C and Basko D M 2013 Raman spectroscopy as a versatile tool for studying the properties of graphene *Nat. Nanotechnol.* **8** 235–46
[19] Lübbe J, Tröger L, Torbrügge S, Bechstein R, Richter C, Kühnle A and Reichling M 2010 Achieving high effective Q-factors in ultra-high vacuum dynamic force microscopy *Meas. Sci. Technol.* **21** 125501
[20] Lübbe J, Doering L and Reichling M 2012 Precise determination of force microscopy cantilever stiffness from dimensions and eigenfrequencies *Meas. Sci. Technol.* **23** 045401
[21] Lübbe J, Temmen M, Rode S, Rahe P, Kühnle A and Reichling M 2013 Thermal noise limit for ultra-high vacuum noncontact atomic force microscopy *Beilstein J. Nanotechnol.* **4** 32–44
[22] Nonnenmacher M, O'Boyle M P and Wickramasinghe H K 1991 Kelvin probe force microscopy *Appl. Phys. Lett.* **58** 2921–3
[23] Weaver J M R and Abraham D W 1991 High resolution atomic force microscopy potentiometry *J. Vac. Sci. Technol.* B **9** 1559–61
[24] Ochedowski O, Kleine Bussmann B, Ban d'Etat B, Lebius H and Schleberger M 2013 Manipulation of the graphene surface potential by ion irradiation *Appl. Phys. Lett.* **102** 153103
[25] Nečas D and Klapetek P 2012 Gwyddion: an open-source software for SPM data analysis *Cent. Eur. J. Phys.* **10** 181–8
[26] Bernal J D 1924 The structure of graphite *Proc. R. Soc. London* A **106** 749–73
[27] Baskin Y and Meyer L 1955 Lattice constants of graphite at low temperatures *Phys. Rev.* **100** 544
[28] Chung D D L 2002 Review graphite *J. Mater. Sci.* **37** 1475–89
[29] Filleter T, Emtsev K V, Seyller T and Bennewitz R 2008 Local work function measurements of epitaxial graphene *Appl. Phys. Lett.* **93** 133117
[30] Temmen M, Ochedowski O, Bussmann B K, Schleberger M, Reichling M and Bollmann T R J 2013 Routes to rupture and folding of graphene on rough 6H-SiC(0001) and their identification *Beilstein J. Nanotechnol.* **4** 625–31
[31] Reichling M, Huisinga M, Gogoll S and Barth C 1999 Degradation of the CaF_2(111) surface by air exposure *Surf. Sci.* **439** 181–90
[32] Miura K, Yamada T, Ishikawa M and Okita S 1999 Apparent contrast of molecularly thin films of water at ionic crystal surfaces *Appl. Surf. Sci.* **140** 415–21
[33] Verdaguer A, Cardellach M and Fraxedas J 2008 Thin water films grown at ambient conditions on BaF_2(111) studied by scanning polarization force microscopy *J. Chem. Phys.* **129** 174705
[34] de Leeuw N H, Parker S C and Rao K H 1998 Modeling the competitive adsorption of water and methanoic acid on calcite and fluorite surfaces *Langmuir* **14** 5900–6
[35] de Leeuw N H, Purton J A, Parker S C, Watson G W and Kresse G 2000 Density functional theory calculations of adsorption of water at calcium oxide and calcium fluoride surfaces *Surf. Sci.* **452** 9–19
[36] de Leeuw N H and Cooper T G 2003 A computational study of the surface structure and reactivity of calcium fluoride *J. Mater. Chem.* **13** 93–101
[37] Foster A S, Trevethan T and Shluger A L 2009 Structure and diffusion of intrinsic defects, adsorbed hydrogen, and water molecules at the surface of alkali-earth fluorides calculated using density functional theory *Phys. Rev.* B **80** 115421
[38] Reischl B, Watkins M and Foster A S 2013 Free energy approaches for modeling atomic force microscopy in liquids *J. Chem. Theory Comput.* **9** 600–8

[39] Li Z *et al* 2013 Effect of airborne contaminants on the wettability of supported graphene and graphite *Nat. Mater.* **12** 925–31
[40] Masel R I 1996 *Principles of Adsorption and Reaction on Solid Surfaces* (New York: Wiley-Interscience)
[41] Russ J C 2006 *The Image Processing Handbook* 5th edn (Boca Raton, FL: CRC Press)
[42] Huang Q, Gaoa W and Caib W 2005 Thresholding technique with adaptive window selection for uneven lighting image *Pattern Recognit. Lett.* **26** 801–8
[43] Otsu N 1979 A threshold selection method from gray-level histograms *IEEE Trans. Syst. Man Cybern.* **9** 62–66
[44] Ratke L and Voorhees P W 2002 *Growth and Coarsening: Ostwald Ripening in Material Processing Engineering Materials and Processes* (Berlin: Springer)
[45] Drucker J 1993 Coherent islands and microstructural evolution *Phys. Rev.* B **48** 18203–6
[46] Boddeti N G, Liu X, Long R, Xiao J, Bunch J S and Dunn M L 2013 Graphene blisters with switchable shapes controlled by pressure and adhesion *Nano Lett.* **13** 6216–21
[47] Lee C, Wei X, Kysar J W and Hone J 2008 Measurement of the elastic properties and intrinsic strength of monolayer graphene *Science* **321** 385–8
[48] Lee C, Wei X, Li Q, Carpick R, Kysar J W and Hone J 2009 Elastic and frictional properties of graphene *Phys. Status Solidi* B **246** 2562–7
[49] Zhang Y and Pan C 2012 Measurements of mechanical properties and number of layers of graphene from nano-indentation *Diamond Relat. Mater.* **24** 1–5
[50] Yue K, Gao W, Huang R and Liechti K M 2012 Analytical methods for the mechanics of graphene bubbles *J. Appl. Phys.* **112** 083512
[51] Bunch J S and Dunn M L 2012 Adhesion mechanics of graphene membranes *Solid State Commun.* **152** 1359–64
[52] Scharfenberg S, Rocklin D Z, Chialvo C, Weaver R L, Goldbart P M and Mason N 2011 Probing the mechanical properties of graphene using a corrugated elastic substrate *Appl. Phys. Lett.* **98** 091908
[53] Yoon T, Shin W C, Kim T Y, Mun J H, Kim T-S and Cho B J 2012 Direct measurement of adhesion energy of monolayer graphene as-grown on copper and its application to renewable transfer process *Nano Lett.* **12** 1448–52
[54] Kang S J, Kim B, Kim K S, Zhao Y, Chen Z, Lee G H, Hone J, Kim P and Nuckolls C 2011 Inking elastomeric stamps with micro-patterned, single layer graphene to create high-performance ofets *Adv. Mater.* **23** 3531–5
[55] Yoo K, Takei Y, Kim S, Chiashi S, Maruyama S, Matsumoto K and Shimoyama I 2013 Direct physical exfoliation of few-layer graphene from graphite grown on a nickel foil using polydimethylsiloxane with tunable elasticity and adhesion *Nanotechnology* **24** 205302
[56] Hallam T, Wirtz C and Duesberg G S 2013 Polymer-assisted transfer printing of graphene composite films *Phys. Status Solidi* B **250** 2668–71